COMPUTER MODELLING OF ALUMINUM-GALLIUM ARSENIDE/GALLIUM ARSENIDE MULTILAYER PHOTOVOLTAICS

BY

MICHAEL BRODERICK WAGNER

B.S., Washington State University, 1984

THESIS

Submitted in partial fulfillment of the requirements
for the degree of Master of Science in Electrical Engineering
in the Graduate College of the
University of Illinois at Urbana-Champaign, 1987

Urbana, Illinois

TABLE OF CONTENTS

ACKNOWLEDGEMENTS

I wish, first, to acknowledge the support and encouragement of my parents, who motivated me to pursue graduate studies.

I would also like to express appreciation to my advisor, J. P. Leburton, for many helpful discussions of the project.

This work was made possible by the support of NASA Grant NAG 3-507.

TABLE OF CONTENTS

1. INTRODUCTION

Space applications are currently the most important role for photovoltaics, and for many years will probably continue to be. As one might expect, design considerations for space-based photovoltaics differ somewhat from considerations for terrestrial photovoltaics. The principal design criteria for space-based photovoltaics are high specific power (i.e., power per unit weight) and good radiation tolerance, which is important since cells in space are exposed to fluences of energetic particles that damage the semiconductor lattice, thereby degrading cell efficiency. Radiation damage is cumulative, so that cells deployed in space have a finite useful lifetime.

1.1. Advantages of III-V Materials for Photovoltaic Applications

Although existing space-based photovoltaics are made exclusively from silicon, III-V compound semiconductors and their ternary alloys show great promise as photovoltaic materials, particularly for space applications. In this regard, they exhibit several advantages over silicon. Available energy gaps of these materials provide a better match to the solar spectrum, allowing higher conversion efficiencies than with silicon. Large-area GaAs heteroface cells with one-sun air mass zero (AM0) efficiencies of 21% have been recently demonstrated [1]. This compares to 15% for silicon cells under the same conditions [2]. Many of the III-V's have a direct energy gap, which permits fabrication of thin-film cells of lighter weight than thick-film devices. The III-V's also exhibit greater tolerance to radiation damage than silicon.

Perhaps the most important advantages of the III-V's are the flexibility provided by their ternary alloy systems, which span a wide range of energy gaps, and the ability to grow multilayer, multi-band-gap structures with these materials. The advent of advanced epitaxial-growth technologies (molecular beam epitaxy and metalorganic chemical vapor deposition) has also made possible a large variety of new artificial materials, known as superlattices, which can be grown with the III-V's. The principal characteristic of a superlattice is one-dimensional band structure periodicity induced by alternating layers of different composition or doping type. The former is referred to as a compositional superlattice and the latter is called a doping superlattice. Individual layers of these structures are typically so thin (particularly for compositional superlattices) that novel quantum effects become important in describing the electronic and optical properties of these materials.

1.2. Viability of Superlattices as Photovoltaic Materials

Compositional superlattices grown from lattice-mismatched materials (known as strained-layer superlattices) have been proposed as an alternative to homogeneous compounds and their alloys for high-efficiency photovoltaics because of lower defect densities [3]. However, compositional superlattices possess localized quantum states caused by carrier confinement in the layers of smallest energy gap. These states tend to promote the capture of energetic minority carriers, enhancing recombination. Once photogenerated minority carriers recombine, they cannot contribute to the output current of the cell. High-efficiency cells require low recombination rates for photogenerated

carriers, which means that materials with long minority-carrier-diffusion lengths are essential. Recent experimental evidence confirms that minority-carrier-diffusion lengths in the direction transverse to the layers of a strained-layer superlattice are in fact quite small [4]. The suitability of compositional superlattices for photovoltaic energy conversion is, therefore, doubtful.

Doping superlattices (sometimes referred to as NIPI crystals) are, at first glance, considerably more interesting as a potential photovoltaic material. Recombination of minority carriers is greatly reduced in NIPI crystals because of an indirect gap in real space between electron states in the conduction band and hole states in the valence band. Photogenerated electrons and holes are spatially separated within picoseconds, allowing them almost no chance to recombine [5]. Thus, NIPI crystals are ideal from the standpoint of short-circuit current. Unfortunately, NIPI crystals are not a viable photovoltaic material because of excessive dark current. The space-charge-recombination contribution to the dark current is proportional to the volume of a structure which is depleted, and NIPI crystals are almost entirely depleted.

1.3. Advantages of Multilayer Structures

Even though superlattices, which are essentially multilayer structures with ultrathin layers, do not appear interesting as potential photovoltaic materials, multilayer structures with thicker layers are of interest for two reasons.

First, the possibility of growing monolithic, multi-band-gap photovoltaics (often referred to as cascade cells) may eventually allow

conversion efficiencies in excess of 30% to be achieved. The concept of cascade cells may be understood in terms of a partitioning of the solar spectrum among two or more subcells of differing energy gaps. The operation of a two-gap cell will be described to illustrate the concept.

The two subcells are epitaxially grown in a vertical stack with the highest-energy-gap subcell on top. Incident solar radiation with energy greater than the upper-subcell energy gap is absorbed by that subcell. Radiation with energy less than the upper-subcell gap and greater than the lower-subcell gap is absorbed by the lower subcell. By selecting the energy gaps of the two subcells to yield an optimal partition of the spectrum, one can, in principle, obtain higher conversion efficiency than is possible with single-gap cells. This is because the average difference between the initial energy of a photogenerated minority carrier and the energy gap of the subcell in which the carrier was excited is smaller when there are two available energy gaps, rather than one. Photoexcited carriers quickly relax to the band edge, so that the excess energy of carriers excited by photons with energy well above the energy gap is lost to lattice heating. In theory, the more energy gaps in a cascade structure, the greater is the attainable efficiency, since the spectrum is partitioned more finely. However, the challenges of fabricating a two-gap monolithic cascade structure have proved sufficiently daunting for present technology. Cascade cells demonstrated to date have yet to exceed efficiencies of the best single-gap cells [6].

The second reason for going to multilayer structures is the possibility of enhancing spectral response (which is the fraction of photoexcited carriers that contribute to the short-circuit current) and

improving radiation tolerance with additional homojunctions in a single-gap cell [26]. By reducing the average distance photoexcited minority carriers must be transported before encountering a junction, the probability of carriers being collected before they recombine is increased.

The collection probability for minority carriers is determined principally by the semiconductor minority-carrier-diffusion length and the distance to a junction. In practice, the designer has little control over diffusion lengths. A compromise must be found between the conflicting requirements of higher doping concentrations, which increase the junction barrier potential (and therefore the open-circuit voltage), and long diffusion lengths for good spectral response, which dictates that impurity concentrations be minimized. Thus, the only available means for improving spectral response is to reduce the average collection distance by increasing the number of junctions.

2. MODELLING

The basic lumped-parameter circuit model of a photovoltaic cell is shown in Figure 1. Operation under one-sun AM0 conditions is assumed, so that it is reasonable to neglect both shunt and series resistances. Shunt resistance effects are important at very low levels of illumination, while series resistance effects are important under high solar concentration [2]. The electrical characteristics of a cell are usually described by three quantities: short-circuit-current density (J_{sc}), open-circuit voltage (V_{oc}), and fill factor (FF), which is defined as the ratio of maximum cell output power to the product of J_{sc} and V_{oc}.

Composite models for multilayer photovoltaics are constructed from the fundamental building block of a current source shunted by a diode. The current source represents photocurrent collected across a junction and the diode represents dark current shunted away from the output by the junction. This simple lumped-parameter model assumes a superposition of photocurrent and dark current. While valid for low-injection conditions, the assumption breaks down under high-injection conditions ($p \simeq n$ in quasi-neutral regions) [7]. However, it will not be necessary to deal with this case for the illumination conditions assumed herein.

2.1. Single-gap Multilayer Structure

The first type of structure to be considered is a single-gap, multilayer cell grown with AlGaAs, in which all junctions are connected in parallel. A schematic cross-sectional view of such a cell is shown in

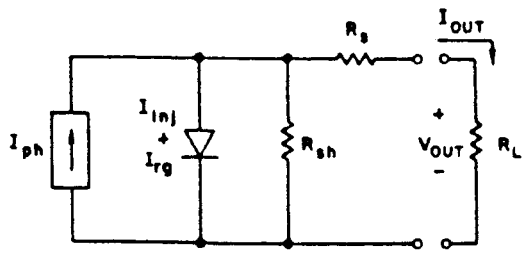

Figure 1. Lumped-parameter circuit model of a single junction photovoltaic cell.

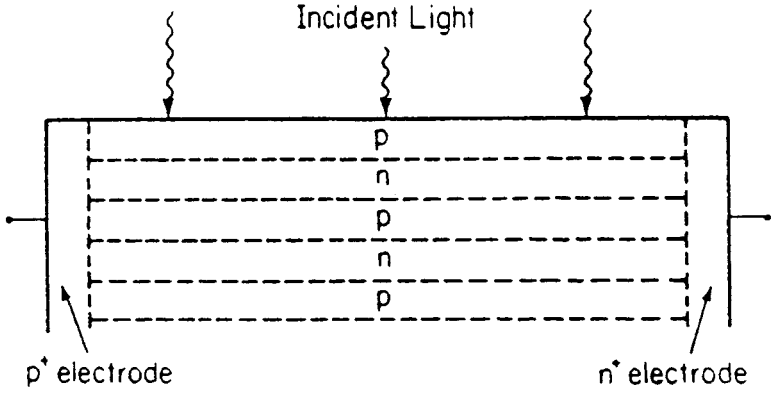

Figure 2. Schematic cross-sectional view of a multijunction, single-gap photovoltaic structure.

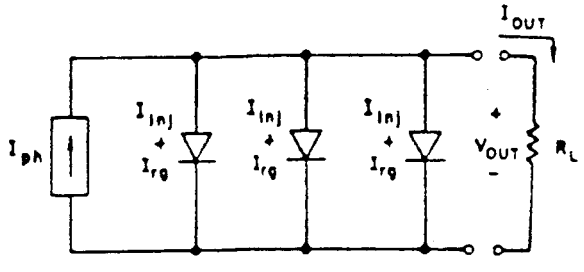

Figure 3. Equivalent circuit used to model multijunction cells.

Figure 2. At the top of the structure is a thin layer of high-energy-gap AlGaAs, known as a window, which allows almost all of the solar spectrum to pass through it without being absorbed. The window provides an interface to the uppermost active layer of the cell (usually called the emitter) with a much lower recombination velocity than would occur at a surface. The structure is essentially a succession of back-to-back p-n junctions, which precludes transport of collected carriers in the direction transverse to the layers. To overcome this problem, heavily doped contact regions that extend vertically through the structure allow transport of collected carriers in the layer planes. These regions are known as selective electrodes since they connect to layers of like doping, while forming reverse-biased junctions (during normal operation) with layers of opposite doping type.

Selective electrodes have been used in other multilayer devices, such as an avalanche photodiode proposed by Capasso [8]. Because they allow collected carriers to be transported in the layer planes, selective electrodes make it possible to incorporate any number of epitaxial layers into the structure (within constraints imposed by the technology used to fabricate the electrodes). Both p- and n-type electrodes are necessary, so that an interdigitated front-surface grid array is required.

Resistive losses, as discussed previously, are assumed negligible, allowing the multilayer structure to be modelled as a composite current source (consisting of the short-circuit-current contributions of each layer) shunted by multiple diodes, which represent the loading effects of the junctions (see Figure 3). The current shunted by the diodes, known as dark current, consists of two principal components: injection and space-charge recombination.

The injection component arises from unbalanced diffusion currents caused by lowering of the junction barrier potential when forward bias is applied. Electrons are injected from the n-side of the junction into the p-side, and holes are injected from the p-side to the n-side. If this component is dominant, the dark current is referred to as "diffusion limited" and the junction can be adequately modelled by the Shockley diode equation.

The other dark-current mechanism is space-charge recombination, which occurs in the depleted region of a junction. This is modelled according to a theory developed by Sah, Noyce, and Shockley [9] for abrupt, symmetric junctions (i.e., equal lifetimes, mobilities, and minority-carrier densities on both sides), and later modified by Choo [10] for asymmetric junctions. The model is simple and convenient to apply: one merely adds a term to the Shockley diode equation to account for the space-charge recombination current. In the AlGaAs alloy system, space-charge recombination will always dominate the injection component when a cell of this material is operating at its maximum-power point [11].

The composite current-voltage (I-V) characteristic of the lumped-parameter model in Figure 3 may be written as follows:

$$J(v)= \sum_{k=1}^{N_L} \{J_{sc_k} - J_{o_k} (e^{\lambda v} - 1)\} - \sum_{m=1}^{N_J} J_{gr_m} \frac{\sinh(\lambda v/2)}{\lambda(v_{b_m} - v)} \qquad (1)$$

where J_{sc_k} is the short-circuit-current contribution of the k^{th} layer; J_{o_k} is the coefficient for the injection-current contribution of the k^{th} layer; N_L is the total number of layers (including the window); J_{gr_m} and

v_{b_m} are the space-charge-recombination coefficient and junction barrier potential, respectively, of the m^{th} homojunction; N_J is the number of homojunctions; and $\lambda=q/k_bT$ is the inverse of the thermal voltage. Note that $N_J= N_L- 2$ for structures considered in this section since the first junction (between the window and emitter) is a heterojunction, not a homojunction.

In the operating regime of interest $v>>k_bT/q$, allowing equation (1) to be approximated by

$$J(v)= \sum_{k=1}^{N_L} \{J_{sc_k} - J_{o_k} e^{\lambda v}\} - \sum_{m=1}^{N_J} J_{gr_m} \frac{e^{\lambda v/2}}{\lambda(v_{b_m} - v)} \tag{2}$$

Simple fixed-point-iteration expressions for open-circuit voltage (v_{oc}) and maximum-power-point voltage (v_{mp}) are easily derived from (2) using the following conditions on J(v):

$$J(v)\Big|_{v=v_{oc}} = 0 \tag{3}$$

$$\frac{d}{dv}\{vJ(v)\}\Big|_{v=v_{mp}} = 0 \tag{4}$$

Expressions for the window, emitter (which is the layer just below the window), and base contributions to the short-circuit and injected currents are well known and have been published elsewhere [2]. Contributions of layers bounded above and below by homojunctions may be derived from the minority-carrier-continuity and current-density equations with the boundary condition of zero excess-carrier density at the depletion-region edges:

$$J_{o_k} = \frac{2qD_n n_i^2}{\alpha^2 L_n^2 - 1} \left[\frac{\cosh((t_k'/L_n) - 1)}{\sinh(t_k'/L_n)} \right] \tag{5}$$

$$J_{sc_k}(\lambda) = \frac{qF_k \alpha L_n}{\alpha^2 L_n^2 - 1} \{\alpha L_n (1 - e^{-\alpha t_k'}) - (1 + e^{-\alpha t_k'}) [\frac{\cosh((t_k'/L_n) - 1)}{\sinh(t_k'/L_n)}]\} \tag{6}$$

where t_k' is the thickness of the k^{th} layer quasi-neutral region; n_i is the intrinsic carrier concentration; N_A, L_n, and D_n are the acceptor concentration, electron diffusion length, and diffusion coefficient, respectively, for a p-doped layer (the corresponding quantities for an n-doped layer are N_D, L_p, and D_p); and q is the charge of an electron. The quantities α and F_k are the absorbtion coefficient and the photon flux incident on the quasi-neutral region of the k^{th} layer. Both depend on the wavelength (λ) of the incident radiation. Thus, in order to determine the total short-circuit current, one must sum over the incident solar spectrum. Data for the AM0 solar spectrum were obtained from reference 12.

In order to accurately determine the total short-circuit current, one must also consider the window-layer and depletion-region contributions. An expression for the window-layer contribution may be found in reference 13. The contribution from the depletion region of the m^{th} homojunction is:

$$J_{sc}^{dr}(\lambda) = qF_m(1 - e^{-\alpha W_m}) \tag{7}$$

where W_m is the width of the depletion region and F_m is the photon flux incident upon it. This equation assumes 100% collection of carriers

photogenerated in the depletion region, which is reasonable since the large space-charge field should rapidly sweep minority carriers across the junction. Note that space-charge recombination need not be considered when computing the short-circuit current because there is no bias across the junction. For notational clarity, it should be pointed out that the depletion-region contributions to short-circuit current are implicitly included in the J_{sc} terms of equation (2).

Spectral data available in the literature are given as a tabulation of flux vs. wavelength, where the flux is integrated over a small interval about each wavelength. Thus, the most convenient method of computing the short-circuit current is to calculate the contributions of all regions for the flux at a given wavelength, starting at the top of the structure and working down, taking into account the reduction in photon flux as the light passes through each region. Total J_{sc} is determined by repeating this procedure for wavelengths across the relevant portion of the solar spectrum, and summing the results. Spectral superposition is valid since the differential equations and boundary conditions governing the photoexcited minority-carrier populations are linear. Simulations discussed in this paper used spectral data from 200 to 900 nm with 10 nm increments. Below 200 nm the solar flux is negligible. The 900 nm upper cutoff represents photon energy just below the energy gap of GaAs.

As mentioned previously, the only III-V alloy system considered in this paper is AlGaAs. This is principally because its properties have been extensively studied and it is lattice-matched to GaAs at all compositions. Mobilities and diffusion lengths are computed as functions

of doping concentration and alloy composition, using empirical relations for the dependence on doping in GaAs [13]. These were modified for AlGaAs by including a polar-optical-phonon scattering term to account for effects of alloy composition [14]. The model used for the absorption coefficient (α) is that described by Hutchby and Fudurich [15], with the exception that effects of the Γ_{15} band are neglected. The energy gap between the valence band and the Γ_{15} band in GaAs is actually much larger (4.6 eV) [16] than the value of 2.9 eV given in reference 15.

Doping profiles are modelled as uniform throughout each layer with abrupt transitions at junctions. Although doping gradients can improve spectral response, the effect is small for cells with a p-doped base [17]. Since all designs considered in this paper assume a p-doped base region, the additional modelling complexity is not worth the trouble for the small increment in efficiency (an improvement of 0.5% AMO was found for n/p heteroface cells with an exponential doping profile [17]). Junction barrier potentials are calculated using Fermi-Dirac carrier statistics.

For all structures, the top layer is assumed to be a 300 Å-$Al_{0.9}Ga_{0.1}As$ window with a surface recombination velocity of 10^6cm/s and interface recombination velocity of 10^3cm/s. The bottom layer (base) is assumed to have a back-surface field (which is essentially a low-high junction) with an effective recombination velocity of 10^4cm/s. An antireflection coating of Si_3N_4 is also included in the model, following reference 18. Grid obscuration is assumed to be 4%, attainable with existing grid-array technology [1].

A simulation program was developed to implement this model which produces cell designs by optimizing layer thicknesses for operating

conditions of one-sun AMO at 300 K. The minimum allowed quasi-neutral region thickness for any layer is 0.1 μm. This constraint assures the validity of the depletion-region approximation. Since the selective-electrode contact regions are assumed to cover only a small fraction of the cell surface, effects of these regions on the minority-carrier distribution may be disregarded, so that the one-dimensional model described above is valid. Doping cannot be realistically optimized without including resistive losses, which provide a lower constraint on concentrations. Efficiencies are not particularly sensitive to variations in doping parameters, however, so that good results may be obtained by assigning near-optimal values.

2.2. Multi-band-gap Structures

A class of multi-band-gap structures consisting of a multilayer AlGaAs upper subcell and a GaAs lower subcell is considered in this section. The upper subcell is essentially the structure modelled in the previous section. This class of structures has been proposed as a possible alternative to conventional cascade cell designs [19]. Some straightforward extensions of the model described in Section 2.1 are all that are necessary to allow the performance potential of these novel cascade cells to be evaluated. There are two cases to be considered, which are determined by how the subcells are electrically interconnected. The first case is a three-terminal configuration with the two subcells sharing a terminal of common polarity. The second case is a two-terminal configuration where the subcells are connected in series. The subcells are assumed to be electrically connected by an epitaxially imbedded

intercell ohmic contact. Series connection imposes the constraint of current matching, so that one would expect somewhat lower efficiencies than for the three-terminal case. The details of modelling these interconnection schemes will be treated in the next two subsections.

2.2.1. Three-terminal Configuration

This interconnection method allows the upper and lower subcells to operate at their individual maximum-power points, which is why it yields the best efficiency of the two methods. However, it is not possible to connect three-terminal devices in series to obtain high output voltages, which are necessary for practical applications. The commercial viability of three-terminal photovoltaics has, therefore, been discounted by many researchers [20-22]. Nevertheless, a possible interconnection technique exists, which may have been overlooked by these authors: one can use complementary pairs (npn and pnp) of three-terminal cells for which the upper-subcell short-circuit current of one is matched to the lower-subcell short-circuit current of the other. This approach, shown schematically in Figure 4, yields a two-terminal output which allows these devices to be incorporated into practical arrays. This concept has the advantage of avoiding the complexities of fabricating a monolithically imbedded intercell ohmic contact between the two subcells, as well as the attendant electrical losses of such a contact. Fabrication of intercell ohmic contacts has proved to be one of the principal stumbling blocks to the success of monolithic cascade cells [21].

Cross-sectional views of two possible three-terminal structures are shown in Figure 5. The first has three layers in the upper subcell,

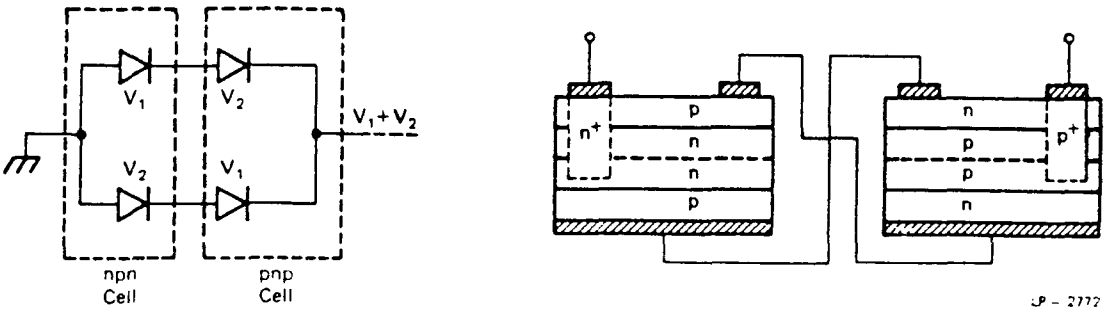

Figure 4. Diagram of complementary-cell interconnection method for three-terminal devices.

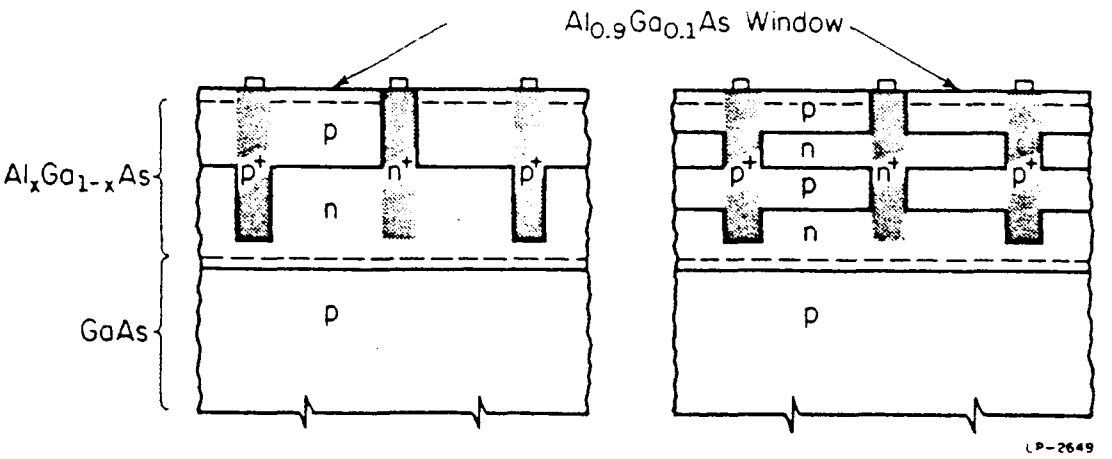

Figure 5. Schematic cross-sections of five- and seven-layer cascade structures. Isotype heterojunctions are represented by dashed lines.

for a total of five layers (the GaAs lower subcell consists of two layers); the second has five layers in the upper subcell, for a total of seven layers. Note that the five-layer structure has one homojunction in the upper subcell, while the seven-layer structure has three. Both structures are of pnp polarity, since it is advantageous from the standpoint of spectral response to have the long electron diffusion length of a p-doped base.

The current-voltage characteristics of these three-terminal devices are represented by an Ebers-Moll model:

$$J_1(v_1,v_2) = J_{sc_1} - J_{o_{11}} e^{\lambda v_1} - J_{o_{12}} e^{\lambda v_2} - \sum_{m=1}^{N_1} J_{gr_m}^{(1)} \left\{ \frac{e^{\lambda v_1/2}}{v_{b_m} - v_1} \right\} \tag{8}$$

$$J_2(v_1,v_2) = J_{sc_2} - J_{o_{21}} e^{\lambda v_2} - J_{o_{22}} e^{\lambda v_1} - \sum_{m=1}^{N_2} J_{gr_m}^{(2)} \left\{ \frac{e^{\lambda v_2/2}}{v_{b_m} - v_2} \right\} \tag{9}$$

where $\lambda = q/k_b T$ and the subscript one refers to the upper subcell. These equations represent a generalization of equation (2), although for conciseness the sums over individual layer contributions to short-circuit and injection currents are not explicitly written out; rather, the J_{sc} terms and J_o coefficients are composite values. Thus, J_{sc_1} is the short-circuit current of the upper subcell and J_{sc_2} is the lower subcell short-circuit current. Coefficients $J_{o_{11}}$, $J_{o_{12}}$, $J_{o_{21}}$, and $J_{o_{22}}$ determine the dependence of the injected component of the dark current on the subcell terminal voltages. Coupling of the current-voltage equations arises from interaction of the injected minority-carrier populations across the heterojunction between the upper and lower subcells. The space-charge-recombination component of the dark current is represented by the

remaining terms. Each summation is over the homojunctions contained in the corresponding subcell. N_1 and N_2 are the numbers of homojunctions in the upper and lower subcells, respectively. For all structures considered in this paper, N_2=1. Note that it is necessary to have a term for each junction because, in general, the barrier potentials (v_{b_m}'s) will not be the same for all junctions in a particular subcell. If they were identical, the voltage dependent terms would factor out and one could simply sum over the J_{gr_m}'s to obtain composite coefficients as in the case of the short-circuit and injected currents.

Contributions of layers in the cascade structure to the short-circuit and injected currents are computed as in Section 2.1 with the exception of the two layers adjacent to the isotype heterojunction separating the upper and lower subcells. These contributions are considerably more complicated to calculate because one must account for interaction between the minority-carrier populations of these layers. The barrier seen by minority carriers at the heterojunction is the junction built-in potential. This holds under all bias conditions since doping concentrations in the layers forming the heterojunction are sufficiently high that junction bias will be effectively zero for typical current densities. Therefore, the boundary conditions on the minority-carrier populations are

$$p_{n_1}/p_{n_2} = \exp[q(E_{F_1} - (\Delta E_v + E_{F_2}))/k_b T] \tag{10}$$

$$D_{p_1} \nabla p_{n_1} = D_{p_2} \nabla p_{n_2} \tag{11}$$

The Fermi levels E_{F_1} and E_{F_2} are measured from the respective valence-band edges. Subscript one denotes the higher-energy-gap layer of the upper subcell. These boundary conditions are nearly identical to those described for low-high junctions [23]. The only difference is the ΔE_v term which must be included in the expression for the junction barrier potential to account for the valence-band-edge discontinuity at the heterojunction. We assume that ΔE_v is 40% of the energy-gap difference, which seems to be the currently accepted rule of thumb [24]. For realistic upper-subcell compositions, the energy-gap difference between the upper and lower subcells is large enough that $p_{n_1}/p_{n_2} \simeq 0$; thus, the precise value of ΔE_v becomes irrelevant. Only for upper-subcell compositions close to GaAs ($x<0.1$) does this value become important.

Once the contributions of all the layers in both subcells have been calculated and the coefficients of equations (8) and (9) determined, these I-V equations must be simultaneously solved for the open-circuit and maximum-power-point voltages of the two subcells. The conditions on the I-V equations for open-circuit voltages are

$$J_1(v_1,v_2)\Big|_{v_1=v_{oc_1},\,v_2=v_{oc_2}} = 0 \tag{12}$$

$$J_2(v_1,v_2)\Big|_{v_1=v_{oc_1},\,v_2=v_{oc_2}} = 0 \tag{13}$$

The condition for maximum-power-point voltages is

$$\frac{d}{dv}\{v_1J_1(v_1,v_2) + v_2J_2(v_1,v_2)\}\Big|_{v_1=v_{mp_1},\,v_2=v_{mp_2}} = 0 \tag{14}$$

Although solving these equations may appear formidable at first, it is actually rather straightforward since the coupling is quite weak, even for an energy-gap difference of zero (i.e., upper and lower subcells both GaAs). The best procedure is to pick reasonable initial values for v_{oc_1} and v_{oc_2}, then solve equation (12) for v_{oc_1} using these initial guesses, holding v_{oc_2} constant. This amounts to solving equation (2) using the fixed-point-iteration expression already mentioned since the injection term for v_{oc_2} can be lumped together with the short-circuit current:

$$J'_{sc_1} = J_{sc_1} - J_{o_{12}} e^{\lambda v_{oc_2}} \tag{15}$$

The value obtained for v_{oc_1} can then be used to find a better approximation to v_{oc_2} by solving equation (13) in the same way. This iterative procedure may then be continued until both v_{oc_1} and v_{oc_2} converge, which usually does not require more than a few iterations. The maximum-power-point voltages may be found by a similar method if one rewrites equation (14) as two separate conditions on $J_1(v_1,v_2)$ and $J_2(v_1,v_2)$, analogous to equation (4).

2.2.2. Two-terminal Configuration

Series interconnection of subcells is the most widely studied configuration for cascade cells [6,20-22,25]. This is because such cells require a minimum number of fabrication steps, which is important for commercially viable devices, and are easy to connect in arrays. The preferred approach is to use a monolithic intercell ohmic contact.

Many approaches have been tried, but all have met with limited success, and none is even close to the performance needed for a practical cascade cell [21]. Nevertheless, for the sake of completeness, it was decided to simulate a series-interconnect configuration for the cascade structure discussed in this paper.

The interconnect is assumed to be electrically and optically lossless, which is a reasonable approximation to the performance that a practical interconnect must achieve. The interconnect is assumed to act as a barrier to minority carriers in the layers adjacent to the interconnect, so that interaction of minority-carrier populations across the heterojunction does not occur in the series configuration. This is physically plausible for a degeneratively doped tunnel-junction interconnect, since the resulting low-high junctions on either side of the heterojunction will act as minority-carrier mirrors. Isolation of the minority-carrier populations means that coupling of the I-V characteristics does not occur. Computation of the subcell I-V characteristics is, therefore, much simpler since each takes the form of equation (2).

The fact that the cells are connected in series, however, introduces a new constraint: the currents flowing in the upper and lower subcells must be identical. This constraint does not affect the computation of the open-circuit voltage (which is simply the sum of the individual subcell v_{oc}'s), but it does change the condition used to determine the maximum-power-point voltage. This condition becomes

$$\frac{d}{dJ}\{J[v_1(J) + v_2(J)]\}\Big|_{v_1=v_{mp_1},\, v_2=v_{mp_2}} = 0 \qquad (16)$$

Note that it is convenient to choose current as the independent variable. The individual subcell terminal voltages must then be calculated as functions of current. Although a closed-form expression for the inverse of equation (2) does not exist, a simple fixed-point-iteration formula may be derived. It is also useful to observe that $v'(J) = (J'(v))^{-1}$, since a closed-form expression for $J'(v)$ is easy to derive.

3. RESULTS AND DISCUSSION

This chapter will be broken into two parts. The first will discuss single-gap multilayer structures, which primarily serves to illustrate how additional junctions can enhance spectral response, especially in the high-energy-gap, low-diffusion-length materials needed for upper subcells of multi-band-gap cascade cells. The second section, on which the most emphasis will be placed, will demonstrate the potential of the novel cascade structures modelled in the preceding chapter.

3.1. Results for Single-gap Multilayer Structures

To illustrate the mechanism by which such multilayer structures can enhance spectral response refer to Figure 6, which shows beginning-of-life (BOL) spectral response curves for three- and four-layer structures. Observe that the knee of the spectral response curve at the red end of the spectrum is much sharper for the four-layer structure. This indicates superior response at the red end of the spectrum, near the energy gap of GaAs. The absorption coefficient for photons of energy near the gap is much smaller than for higher energy photons, hence the low-energy photons tend to penetrate much deeper into the structure before being absorbed. However, most photons are absorbed near the surface, so the single junction of the three-layer structure must be placed close to the surface. The additional junction of the four-layer structure may be placed much deeper so that carriers photoexcited by low-energy photons are closer to a junction. This substantially increases their probability of being collected. The relative contribution of the

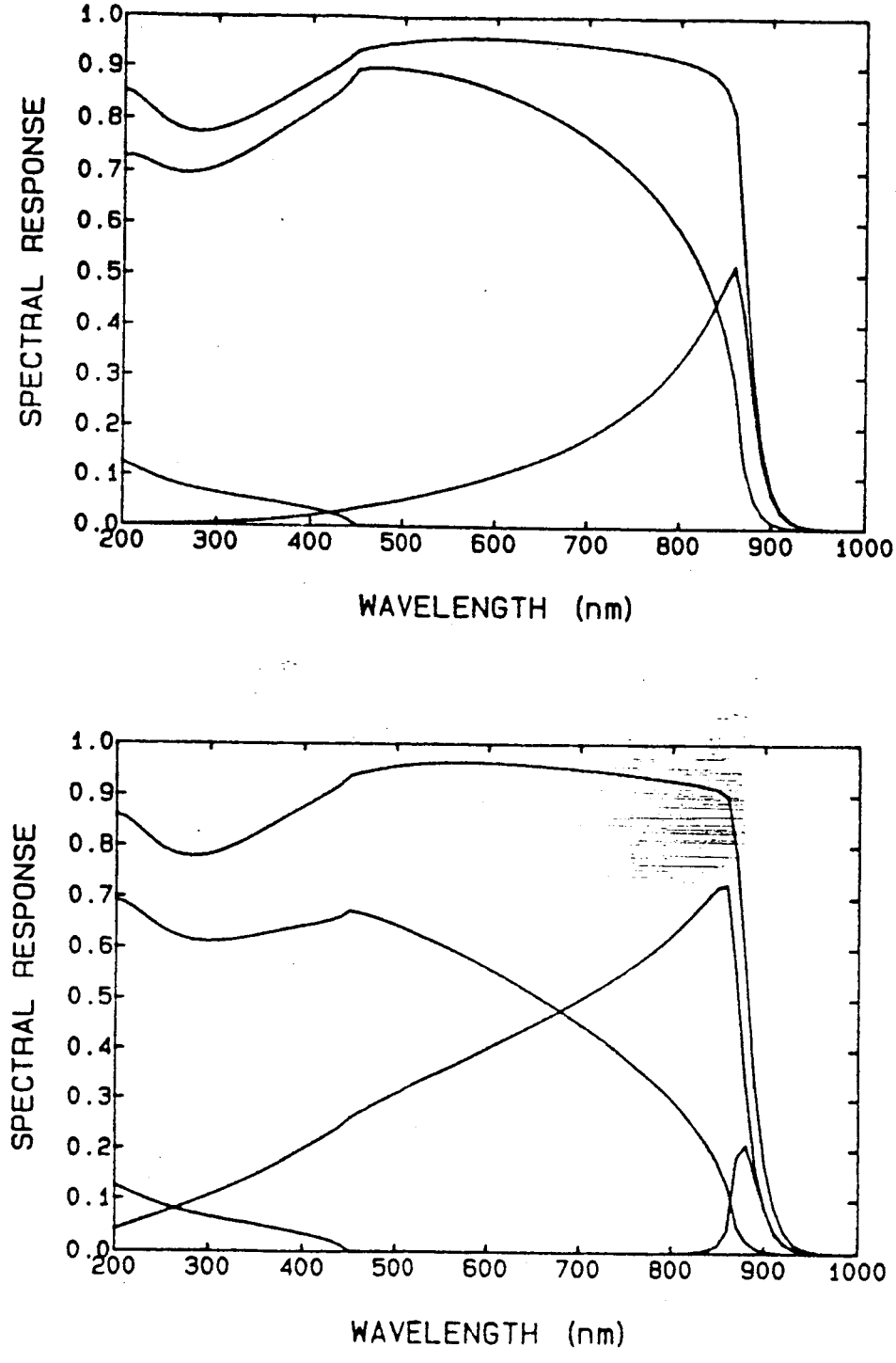

Figure 6. Spectral response curves of three- and four-layer single-gap structures. Individual layer contributions are shown as well as overall spectral response.

base region in the four-layer structure is substantially smaller than the relative contribution of the base in the three-layer structure. Minimizing the proportion of the spectral response contributed by the base is desirable since bulk recombination losses occur mostly in this region.

The curves in Figure 7 show how J_{sc} and v_{oc} are affected by the number of layers in the cell structures at two different alloy compositions. As the number of layers is increased, bulk recombination losses become negligible and J_{sc} approaches a limiting value determined primarily by grid, reflection, and window losses. The open-circuit voltage decreases steadily with increasing numbers of layers because of dark-current contributions of the additional junctions, which load the output. The fill factor also drops, but its fractional decrease is smaller than that of v_{oc}. This behavior illustrates an important phenomenon: a trade-off between spectral response and dark current. The trade-off produces a peak in efficiency at four layers as shown in Figure 8. Note that the largest increase in efficiency over a three-layer cell occurs for an AlAs mole fraction of x=0.4. This is because the shorter minority-carrier-diffusion lengths associated with higher mole fractions of AlAs allow a greater margin for improved spectral response. Multilayer structures therefore appear to be most advantageous for the upper subcells of multi-band-gap cells, which require such high-energy-gap alloys.

Radiation tolerance is also improved by the incorporation of additional layers. Figure 9 shows the effects of degrading diffusion lengths by a factor of five. The four-layer structures yield dramatic improvements in efficiency at all mole fractions shown.

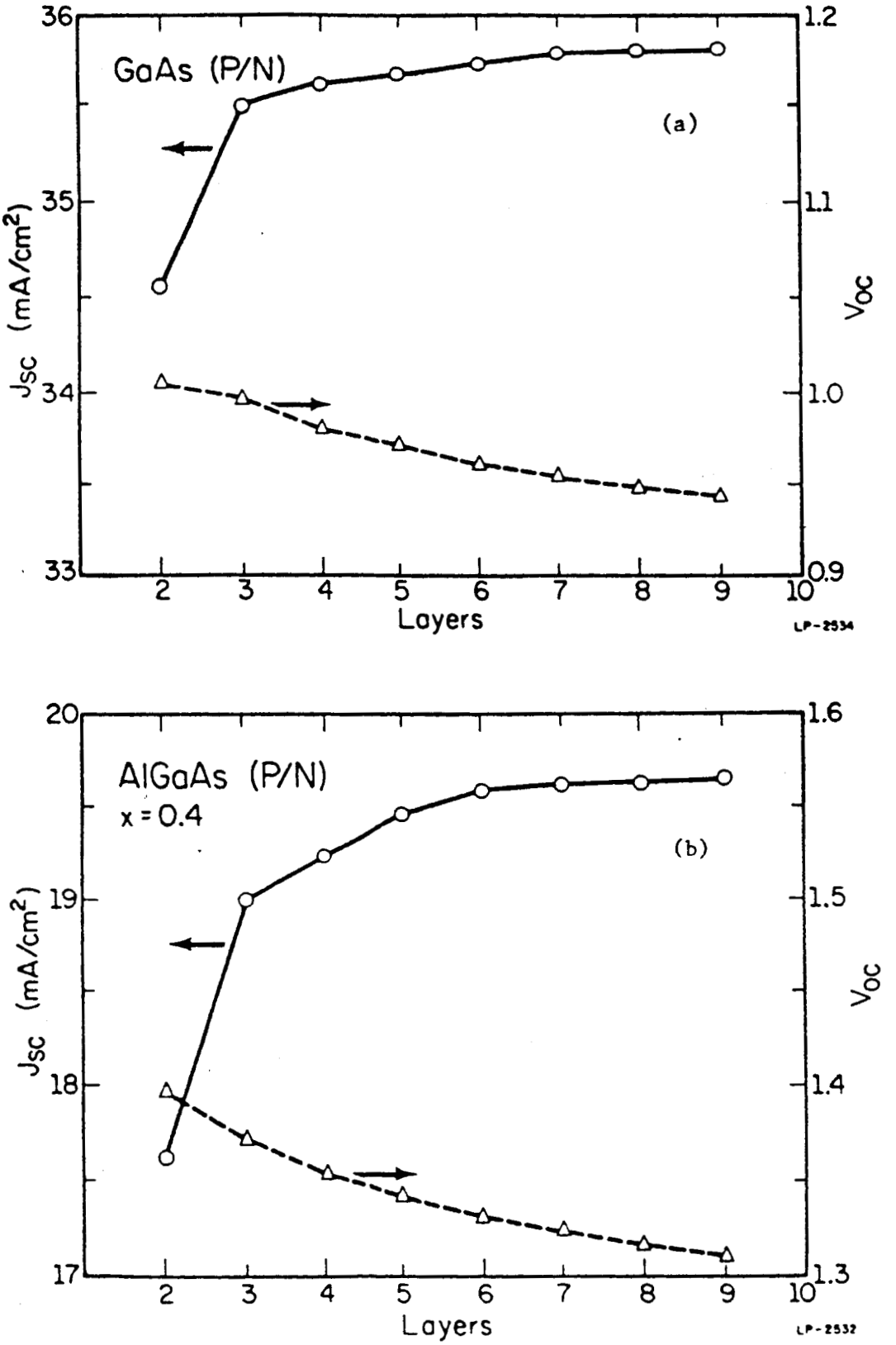

Figure 7. Open-circuit voltage and short-circuit current trends for a) GaAs and b) $Al_{0.4}Ga_{0.6}As$ cells. These curves show the trade-off between spectral response and dark current.

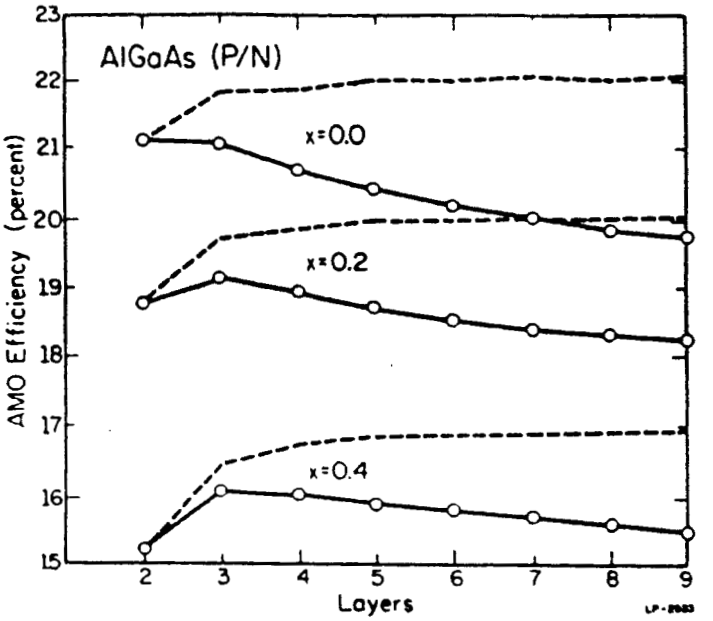

Figure 8. Performance of cell designs optimized for one-sun AMO at 300 K. The dashed curves show efficiencies that would be achieved if space-charge recombination were suppressed.

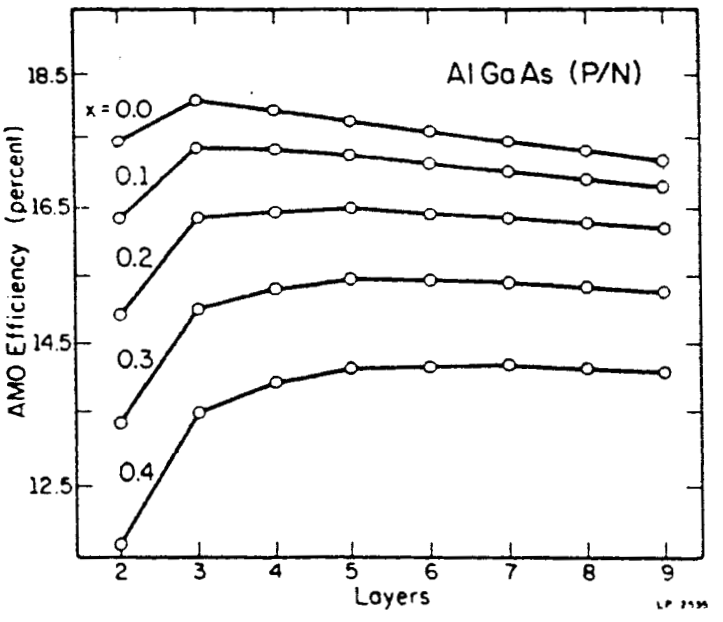

Figure 9. Performance of radiation-damaged cells optimized for end-of-life efficiency. Diffusion lengths were reduced by a factor of five to simulate effects of radiation damage.

3.2. Results for Multi-band-gap Structures

The preceding section demonstrated that one or two extra layers are beneficial to the performance of a single-gap cell, but that many additional layers will not further increase performance; rather, they will begin to degrade it because of their dark-current contributions. Thus, one would expect that the multilayer upper subcell of the cascade structure should have at most five layers (two more than the standard window, emitter, base structure), which corresponds to a seven-layer structure (since the GaAs lower subcell consists of two layers). It is desirable to use an odd number of layers, so that both the emitter of the upper subcell and the base of the lower subcell are p-doped to take advantage of the long electron diffusion length. Thus, only five- and seven-layer structures were studied in detail.

Efficiencies of the optimized cascade structures with the three-terminal configuration vary gradually with upper subcell composition (Figure 10). Broad peaks occur at mole fraction x=0.36 (corresponding to an energy gap of about 1.8 eV) for both the five- and seven-layer structures with maximum BOL one-sun AM0 efficiencies predicted to be slightly in excess of 26%. This contrasts with the rather critical dependence of efficiency on energy-gap selection for series cascade cells, which is a consequence of the current-matching requirement. Theoretically, higher efficiencies could be obtained from a two-gap cascade cell if a lower subcell of energy gap smaller than that of GaAs were used; however, this would require abandoning a lattice-matched alloy system, since none exists which spans the range of optimal energy gaps for the two-gap system [25]. Experiments with lattice-mismatched systems

to date have not yielded very impressive efficiencies; the highest efficiency obtained is 13.6% under one-sun AM1.5 conditions [22] (the AM0 efficiency would be even smaller).

The dashed curves in Figure 10 show that efficiencies approach 30% if space-charge recombination is suppressed. The two sets of efficiency curves (with and without space-charge recombination) diverge as the mole fraction of AlAs in the upper subcell increases. Contrary to what one might initially expect, most of the divergence results not from the upper-subcell contribution but rather from that of the lower subcell. The key to understanding this behavior is the effect on dark current of the total illumination absorbed by a cell. The dark current is proportional to J_{sc} and inversely proportional to maximum power point voltage (V_{mp}). Dark current at V_{mp} is also proportional to the diode ideality factor, so that changes in illumination have a greater effect on the dark current when the space-charge component is dominant, which is always the case for GaAs and AlGaAs cells at V_{mp}. As the upper subcell bandgap increases, its J_{sc} decreases and V_{mp} increases. This tends to reduce space-charge recombination dark current, which would cause convergence. But this effect is offset by increasing dominance of the space-charge recombination dark current component caused by changing materials parameters (carrier lifetimes and intrinsic carrier concentration). However, divergence due to increasing illumination is quite apparent in the lower subcell, which is of fixed composition.

Although the predicted BOL efficiencies of the five- and seven-layer designs are nearly identical, their degradation rates upon exposure to radiation are quite different. This may be seen from Figure 11, which

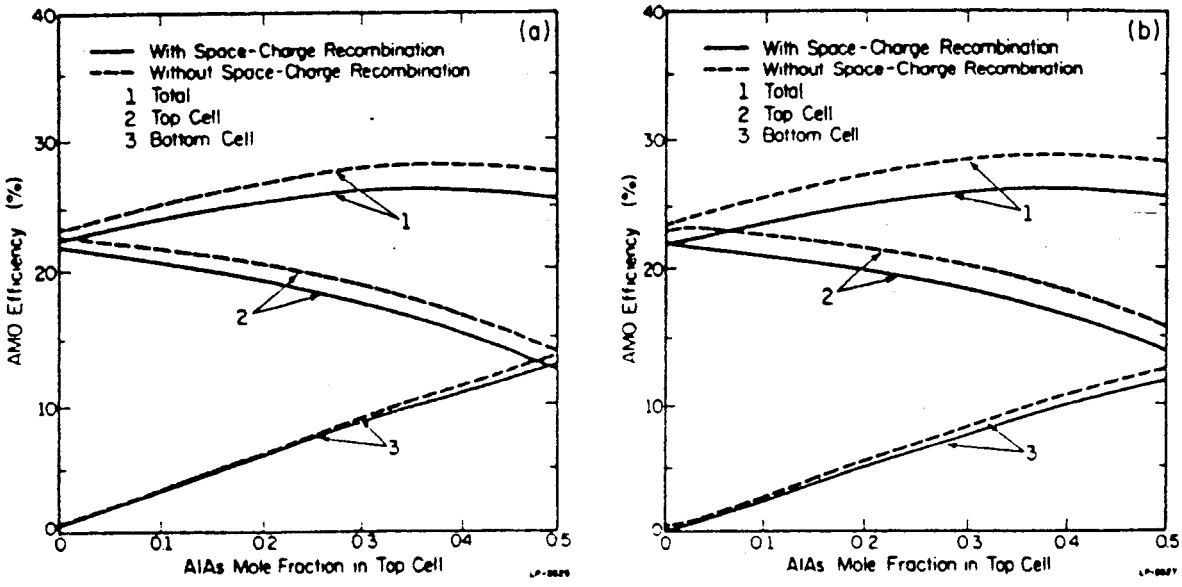

Figure 10. Performance of a) five-layer and b) seven-layer structures as a function of upper subcell composition under one-sun AMO illumination.

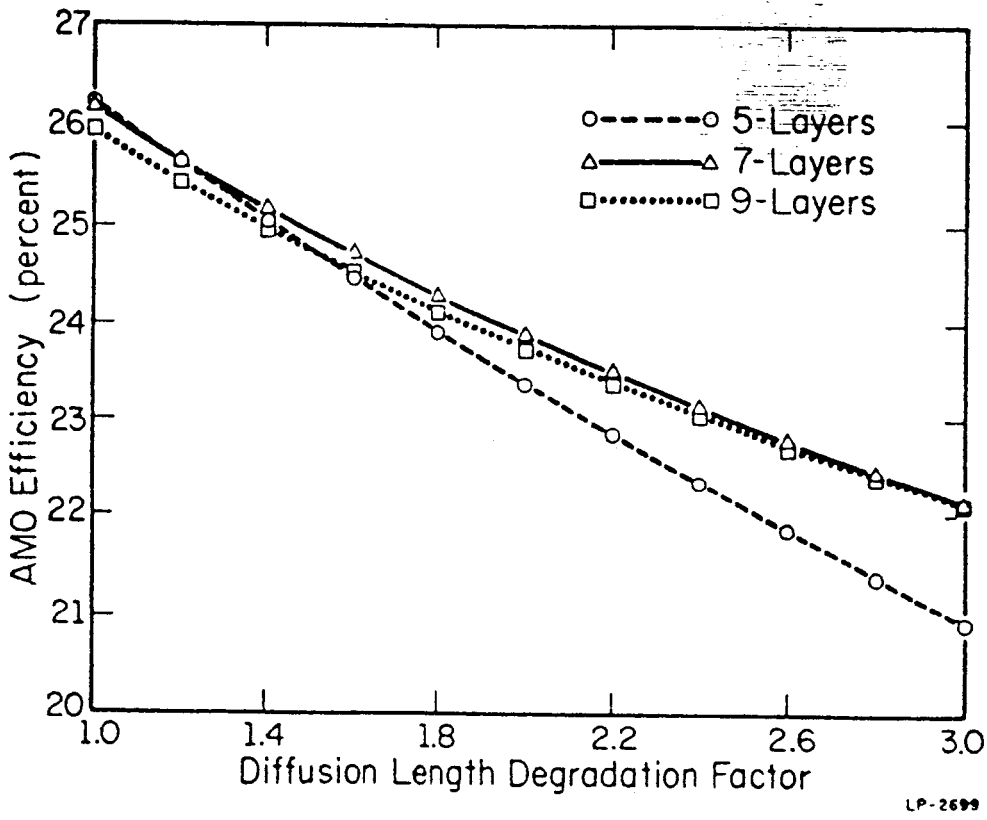

Figure 11. Effects of radiation damage on five-, seven-, and nine-layer cascade structures. Accumulating lattice damage is simulated by increasingly large diffusion-length reductions.

shows the effect of a uniform reduction in diffusion lengths on their efficiencies. Even after substantial degradation, efficiencies of these structures remain well above BOL efficiencies of GaAs heteroface cells. Also included is a curve showing the degradation behavior of a nine layer structure, which is seen to be quite similar to that of the seven layer structure. Thus, there is seen to be no advantage in going beyond seven layers.

The seven layer structure might seem to present a problem for series resistance because of unusually thin layers. In fact, the upper subcell emitter is about 0.3 μm, which is roughly half the emitter thickness of the five layer structure. However, the effect of doubled emitter sheet resistance is mitigated by current sharing among the three upper-subcell homojunctions. The top homojunction carries three-quarters of the upper-subcell current, reducing emitter joule losses to half of what the losses would be if that junction carried the entire subcell current.

4. CONCLUSIONS

The cascade cells modelled in this thesis offer an alternative to conventional series cascade designs that require a monolithic intercell ohmic contact. Selective electrodes provide a simple means of fabricating three-terminal devices, which can be configured in complementary pairs to circumvent the attendant losses and fabrication complexities of intercell ohmic contacts. Moreover, selective electrodes allow incorporation of additional layers in the upper subcell which can improve spectral response and increase radiation tolerance.

Realistic simulations of such cells operating under one-sun AMO conditions show that the seven-layer structure is optimum from the standpoint of beginning-of-life efficiency and radiation tolerance. Projected efficiencies exceed 26%. Under higher concentration factors, it should be possible to achieve efficiencies beyond 30%. However, to simulate operation at high concentration will require a model for resistive losses. Overall, these devices appear to be a promising contender for future space applications.

REFERENCES

[1] J. G. Werthen, G. F. Virshup, C. W. Ford, C. R. Lewis, and A. C. Hamaker, "21% (One-sun Air Mass Zero) 4 cm^2 GaAs Space Solar Cell," Appl. Phys. Lett., vol. 48, pp. 74-75, 1986.

[2] H. J. Hovel, "Solar Cells," Semiconductors and Semimetals, vol. 11, R. K. Willardson and A. C. Beers, Eds., New York: Academic Press, 1975.

[3] R. J. Chaffin, G. C. Osbourn, L. R. Dawson, and R. M. Biefeld, "Strained Superlattice, Quantum Well, Multijunction Photovoltaic Cell," Proc. 17th IEEE Photovoltaic Spec. Conf., New York: IEEE, 1984, pp. 743-746.

[4] P. L. Gourley, J. J. Wiczer, T. E. Zipperian, and L. R. Dawson, "Diffusion Dynamics of Holes in InGaAs/GaAs Strained-layer Superlattices," Appl. Phys. Lett., vol. 49, pp. 100-102, 1986.

[5] G. H. Dohler, "NIPI Doping Superlattices--Metastable Semiconductors with Tunable Properties," J. Vac. Sci. Technol., B, vol. 1, pp. 278-284, 1983.

[6] M. F. Lamorte and D. H. Abbot, "Window Losses and Current-Mismatch Computer Modelling Studies in AlGaAs-GaAs Cascade Solar Cell," IEEE Trans. Electron Devices, vol. ED-30, pp. 1313-1322, 1983.

[7] F. A. Lindholm, J. G. Fossum, and E. L. Burgess, "Application of the Superposition Principle to Solar-Cell Analysis," IEEE Trans. Electron Devices, vol. ED-26, pp. 165-171, 1979.

[8] F. Capasso, "The Channeling Avalanche Photodiode: A Novel Ultra-Low-Noise Interdigitated p-n Junction Detector," IEEE Trans. Electron Devices, vol. ED-29, pp. 1388-1393, 1982.

[9] C. T. Sah, R. N. Noyce, and W. Shockley, "Carrier Generation and Recombination in P-N Junctions and P-N Junction Characteristics," Proc. of the IRE, vol. 45, pp. 1228-1243, 1957.

[10] S. C. Choo, "Carrier Generation-Recombination in the Space-Charge Region of an Asymmetrical P-N Junction," Solid-State Electron., vol. 11, pp. 1069-1077, 1968.

[11] H. J. Hovel, "The Effect of Depletion Region Recombination Currents on the Efficiencies of Si and GaAs Solar Cells," Proc. 10th IEEE Photovoltaic Spec. Conf., New York: IEEE, 1973, pp. 34-39.

[12] C. E. Backus, ed., Solar Cells, New York: IEEE, 1976, p. 2.

[13] C. Goradia and M. Ghalla-Goradia, "Near-Optimum Design of GaAs-Based Concentrator Space Solar Cells for 80°C Operation," Proc. 17th IEEE Photovoltaic Spec. Conf., New York: IEEE, 1984, pp. 56-62.

[14] J. E. Sutherland and J. R. Hauser, "A Computer Analysis of Heterojunction and Graded Composition Solar Cells," IEEE Trans. Electron Devices, vol. ED-24, pp. 363-372, 1977.

[15] J. A. Hutchby and R. L. Fudurich, "Theoretical Analysis of AlGaAs-GaAs Graded Band-gap Solar Cells," J. Appl. Phys., vol. 47, pp. 3140-3151, 1976.

[16] M. L. Cohen and T. K. Bergstresser, "Band Structures and Pseudopotential Form Factors for Fourteen Semiconductors of the Diamond and Zinc-Blende Structures," Physical Review, vol. 141, pp. 789-796, 1966.

[17] H. C. Hamaker, "Computer Modelling Study of the Effects of Inhomogeneous Doping and/or Composition in GaAs Solar Cell Devices," J. Appl. Phys., vol. 58, pp. 2344-2351, 1985.

[18] K. Mitsui, S. Yushida, T. Oda, M. Kato, Y. Yukimoto, and S. Matsuda, "A High Quality AR coating for AlGaAs/GaAs Solar Cells," Proc. 17th IEEE Photovoltaic Spec. Conf., New York: IEEE, 1984, pp. 106-11.

[19] M. Wagner and J. P. Leburton, "Proposal for Superstructure-Based High Efficiency Photovoltaics," Appl. Phys. Lett., vol. 49, pp. 886-888, 1986.

[20] J. C. C. Fan, B-Y. Tsaur, and B. J. Palm, "Optimal Design of High-Efficiency Tandem Cells," Proc. 16th IEEE Photovoltaic Spec. Conf., New York: IEEE, 1982, pp. 692-701.

[21] J. A. Hutchby, R. J. Markunas, M. L. Timmons, P. K. Chaing, and S. M. Bedair, "A Review of Multijunction Concentrator Solar Cells," Proc. 18th IEEE Photovoltaic Spec. Conf., New York: IEEE, 1985, pp. 20-27.

[22] C. R. Lewis, C. W. Ford, G. F. Virshup, B. A. Arua, R. T. Green, and J. G. Werthen, "A Two-Terminal, Two-Junction Monolithic Cascade Solar Cell in a Lattice-Mismatched System," Proc. 18th IEEE Photovoltaic Spec. Conf., New York: IEEE, 1985, pp. 556-561.

[23] M. P. Godlewski, C. R. Baraona, and H. W. Brandhorst, Jr., "Low-High Junction Theory Applied to Solar Cells," Proc. 10th IEEE Photovoltaic Spec. Conf., New York: IEEE, 1973, pp. 40-49.

[24] W. I. Wang, "On the Band Offsets of AlGaAs/GaAs and Beyond," Solid-State Electron, vol. 29, pp. 133-139, 1986.

[25] M. F. Lamorte and D. H. Abbott, "Computer Modeling of a Two-Junction Monolithic Cascade Solar Cell," IEEE Trans. Electron Devices, vol. ED-27, pp. 231-249, 1980.

[26] M. Wagner and J. P. Leburton, "Superstructures and Multijunction Cells for High Efficiency Energy Conversion," Proc. 18th IEEE Photovoltaic Spec. Conf., New York: IEEE, 1985, pp. 157-160.